Solar Energy Materials & Solar Cells 238 (2022) 111654

Contents lists available at ScienceDirect

Solar Energy Materials and Solar Cells

journal homepage: www.elsevier.com/locate/solmat

Experimental study on storage performance of packed bed solar thermal energy storage system using sintered ore particles

Zhenya Lai, Hao Zhou *, Mingxi Zhou, Laiquan Lv, Hanxiao Meng, Kefa Cen

State Key Laboratory of Clean Energy Utilization, Institute for Thermal Power Engineering, Zhejiang University, Hangzhou, 310027, China

ARTICLE INFO

Keywords:
Thermal energy storage
Sintered ore particle
Packed bed
Thermal performance
Air resistance characteristics

ABSTRACT

To cope with the mismatch between solar energy generation and demand, developing thermal energy storage systems is necessary. Due to its low construction and operating costs and wide operating temperature range, the packed bed sensible heat storage system using air as the heat transfer fluid is becoming more and more popular. This paper proposes to use sintered ore particles as a sensible heat storage material. An experimental study is conducted to investigate the air resistance characteristics and thermal behavior of the sinter bed. Moreover, the effects of particle size, charging temperature, air flow and cycle times on storage performance of the bed are studied. The results show that the sinter bed has good thermal performance. The specific heat of the sinter is 0.86–0.98 J/g/°C in the range of 200–380 °C, which increases as the temperature rises. When the thermal storage system enters a stable operation state, the cycle efficiency of the sinter bed can reach 66.78%. In addition, due to the unique production process, sinter has the potential to improve its thermal properties by optimizing the ratio of raw materials and/or adding other auxiliary materials.

1. Introduction

Due to the depletion of conventional fossil energy and the aggravation of environmental pollution, renewable energy sources are becoming increasingly important. Solar energy has the most remarkable development potential in renewable energy sources [1]. However, solar energy is intermittent and unstable. Fortunately, thermal energy storage (TES) system can compensate for the mismatch between energy production and demand [2], making the continuous use of solar energy possible.

TES can be subdivided into sensible heat, latent heat, and thermochemical energy storage. Due to its low construction and operating costs and wide operating temperature range [3], many scholars have recently focused on the packed bed sensible heat storage system using air as the heat transfer fluid. Choosing low-cost and high-efficiency energy storage materials is the key to sensible heat storage research [4].

Rock has been extensively studied [5–15] as an energy storage material due to its availability. Meier et al. [5] conducted early research on packed bed energy storage systems, laying the foundation for subsequent research. They used the models experimentally verified to predict the thermal stratification, bed pressure drop and wall heat dissipation during charging. Okello et al. [6] experimentally investigated the thermal de-stratification in rock bed and discovered that the short storage tank has a higher heat loss rate than the long storage tank. Further study is needed to explore the possibility of more complex storage configurations that can meet different applications. Liu et al. [7] experimentally studied the heat storage and transfer characteristics of rock beds under low pressure and supercritical pressure. Chai et al. [8] conducted experiments to examine the effects of airflow directions and charging temperatures on the thermal performance of the closed-loop energy storage system. The only drawback is the low charging temperature (75–145 °C). Zanganeh et al. [9] developed a dynamic numerical model for fluid and solid phases with thermophysical properties varying in the range of 20–650 °C. Hänchen et al. [10] numerically studied the effects of bed size, the mass flow rate of fluid, particle diameter, and storage material on the energy storage characteristics of the system. The results reveal that the most relevant property of storage materials is volumetric heat capacity, while the thermal conductivity has only a slight effect. Mawire et al. [11] evaluated the applicability of different indicators for thermal stratification in an oil/pebble bed TES system. Schlipf et al. [12] experimentally studied the thermal behavior of three kinds of small size rock particles in a horizontal packed bed storage system. The small particles can form sharp thermocline layers. The research method of thermocline behavior used in this paper provides a reference for the subsequent research on thermocline characteristics.

* Corresponding author.
E-mail address: zhouhao@zju.edu.cn (H. Zhou).

https://doi.org/10.1016/j.solmat.2022.111654
Received 25 May 2021; Received in revised form 15 December 2021; Accepted 13 February 2022
Available online 16 February 2022

Nomenclature

A	study dependent constants
B	study dependent constants
c_{pair}	specific heat capacity of air, J/(kg·K)
d	particle diameter, m
E_{input}	input energy, J
E_{pump}	pumping energy, J
G	air mass flow rate per unit cross section, kg/(m^2·s)
g	gravitational acceleration, 9.81 m/s^2
H	bed height, mm
I	number of sinter layers
i	sinter layer
m	air mass flow, kg/s
Nu	Nusselt number
$Q_{release}$	instantaneous amount of energy released from the packed bed, J
Q_{stored}	instantaneous amount of energy stored in the packed bed, J
r	internal radius of the tank, mm
S	internal cross-sectional area of the tank, m^2
S_{pipe}	internal cross-sectional area of the pipe, m^2
Str	stratification number
T	temperature, °C
t	time, s
T′	air temperature at the outlet of electric air heater, °C
T_{in}	air temperature at the inlet of the tank, °C
T_{ini}	initial temperature of the sinter bed at t = 0, °C
T_{out}	air temperature at the outlet of the tank, °C
U	air superficial velocity in the tank, m/s
V	air flow, m^3/h
v_{pipe}	air velocity in the pipe, m/s
Xi	the ith variable
x	radial position inside the tank, mm
y	axial position inside the tank, mm

Greek symbols

Δp	pressure drop over the bed, Pa
Δy	distance between temperature sensors, mm
δR	uncertainty in the result, generic
ε	voidage of sinter bed
$\eta_{charging}$	charging efficiency
$\eta_{discharging}$	discharging efficiency
η_{cycle}	overall cycle efficiency
θ	dimensionless temperature
μ	dynamic viscosity of air, Pa·s
ρ_a	apparent density of the sintered ore particles, kg/m^3
ρ_{air}	air density, kg/m^3
ρ_b	bulk density of the sintered ore particles, kg/m^3
ρ	density of the sintered material, kg/m^3
φ	porosity of the sintered ore particles
Φ	particle sphericity

Nem's et al. [13–15] built a storage system with granite particles and experimentally studied the influence of granite shape and particle size on storage efficiency. However, the author filled a relatively small container with relatively large particles, which is not conducive to the detailed study of the thermal behaviors in the bed.

Many scholars favor alumina/ceramic materials because of their higher thermal conductivity [16–23]. Nicolas et al. [16] designed a horizontally arranged square-section storage device, which could be flexibly applied to various heat sources. Touzo et al. [17] built a horizontal containerized storage system, which could recover up to 90% of the heat at a discharge threshold temperature of 200 °C. The system is an industrial-scale TES with a storage capacity of 1.9 MWh_{Th} at 525 °C, which validates the performances of a commercial TES operating in actual conditions. To notably increase the dispatchability of Concentrated Solar Plant (CSP), the author needs to develop the storage system operating at higher temperatures (above 1000 °C). Al-Azawii et al. [18] built a horizontally arranged, radial-flow storage device. Compared with the traditional axial flow, the radial flow method could increase the storage capacity from 1076.6 MJ to 1148.3 MJ and the storage efficiency from 75.3% to 80.3%. Daschner et al. [19] built a storage device in the form of a vertical tank. The storage material was filled between the inner tank and the outer shell, and the heat transfer fluid flowed in radially. The experimental results show that the system cycle efficiency exceeds 92% and show the high practical application potential in a wide temperature range. Wang et al. [20] experimentally studied the heat transfer characteristics of a storage system using honeycomb ceramics and verified the applicability of honeycomb ceramics as storage material. Yang et al. [21] experimentally and numerically studied the thermocline degradation in the standby process using a pilot-scale packed bed storage system. The study illuminated well the heat transfer mechanisms during the standby stage and indicated that thermal diffusion and heat loss contribute more to the thermocline degradation than natural convection. Therefore, adopting solidfifillers with low conductivity, better insulating the tank walls both lateral and top, fully charging the solid bed are suggested to help maintain a good and stable stratification during the standby stage. Cascetta et al. [22] experimentally studied the temperature distribution of a packed bed storage system in a charging and discharging cycle, and analyzed the influence of wall heat dissipation on the radial temperature distribution. However, this paper does not carry out the tests under wider operating conditions. Meanwhile, a two-dimensional numerical model considering the effect of wall heat dissipation needs to be developed. Cascetta et al. [23] carried out experimental and numerical simulation studies on the cyclic thermal behavior of an air-alumina ball packed bed. The effects of cut-off threshold temperature and cycle times on energy storage characteristics are studied in detail.

In addition, Agrawal et al. [1] and Gautam et al. [24] used concrete as energy storage material. To reuse the waste, Kocak et al. [25,26] characterized the demolition wastes and studied their applicabilities as sensible heat storage material.

In summary, the materials used by scholars are mainly concentrated in rocks, ceramics/alumina, concrete, and reprocessed and shaped waste materials in the field of sensible heat packed bed energy storage. So far, there is no relevant research using sintered ore particles as sensible heat storage materials. As the primary raw material of the blast furnace, sintered ore particle has low cost, high-temperature resistance, high strength, and is environmentally friendly and non-toxic. Moreover, due to the unique production process, the sinter can improve further its thermal properties by optimizing the ratio of raw materials and/or adding other auxiliary materials.

Considering the above advantages of sinter and its own background of waste heat utilization in sinter cooling bed [27–31], sintered ore particle is used as the sensible heat storage material in the present study. An air/sinter-bed TES test bench was built to study the storage performance of the sinter bed. JPU (Japanese Permeability Units), a permeability index widely used in the sintering field, is introduced to study the airflow resistance characteristics of sinter beds with different particle sizes. The effects of particle size, charging temperature, air flow, and cycle times on the thermal performances of the bed are studied. The dimensionless index Str number is introduced to study the stratification characteristics of the sinter bed.

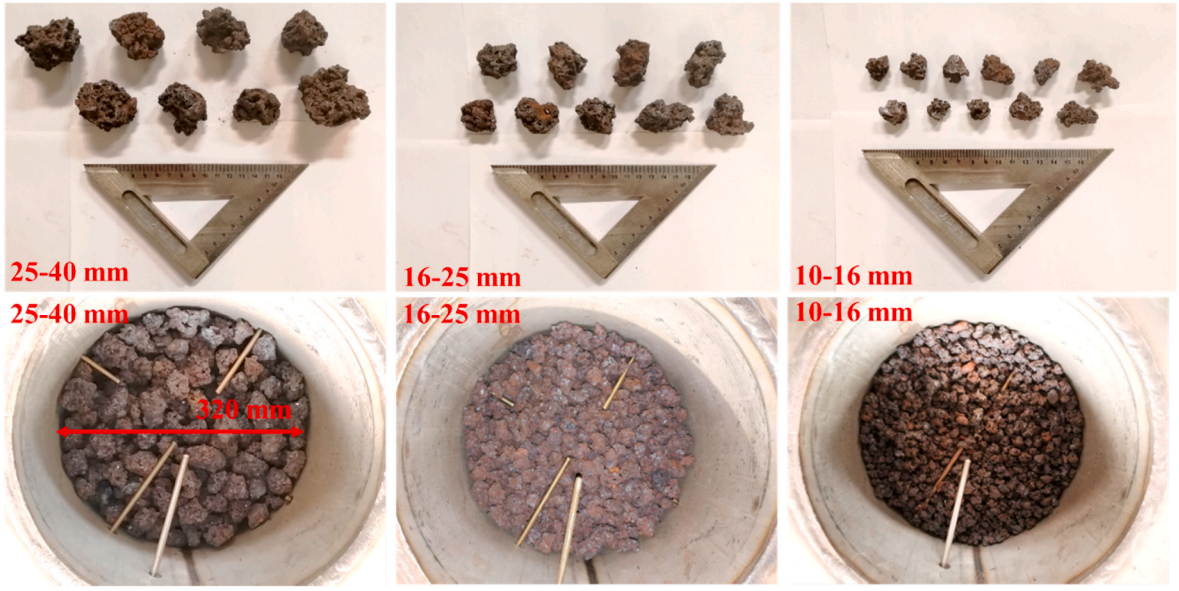

Fig. 1. Sintered ore particles and thermocouple layout inside the storage tank.

Table 1
Measurement results of sinter bed properties.

Particle size	25–40 mm	16–25 mm	10–16 mm
Apparent density ρ_a (kg/m^3)	3600	3688	3727
Density ρ (kg/m^3)	4547		
Porosity of the sintered ore particles φ	0.208	0.189	0.180
Bulk density ρ_b (kg/m^3)	1380	1476	1605
Voidage of packed bed ε	0.617	0.600	0.569

2. Sinter bed properties

The sinters were from ZJU-BHP Billiton Joint Center for Sinter Research. They were crushed and sieved into 25–40 mm, 16–25 mm, and 10–16 mm, as shown in Fig. 1. The apparent densities of sintered ore particles were measured using the Archimedes drainage method [18]. The density of the sintered material was obtained with AccuPyc 1340 automatic true density analyzer. Before the measurement, the sintered ore particles were first crushed into powders of about 75 μm using a coal mill. The bulk density of sinter particles was calculated by dividing the mass of particles in the storage tank by the volume occupied by the bed. The porosity φ of the sinters and the voidage ε of the sinter bed were calculated by formulas (1) and (2), respectively. In the present work, the porosity φ is the ratio of the volume of the pore inside sinter particles to the total volume of sinter particles in the natural state. It is aimed at sinter particles and focuses on the pores inside the particles. However, the voidage ε is the ratio of the volume of the pore between particles in the sinter bed to the total volume of the sinter bed. It is aimed at the packed bed using sinter particles, focusing on the pores between particles.

$$\varphi = 1 - \frac{\rho_a}{\rho} \tag{1}$$

$$\varepsilon = 1 - \frac{\rho_b}{\rho_a} \tag{2}$$

Table 1 gives the results of sinter density. It can be seen that the apparent density of sinter particles decreases as particle diameter increases [18]. The leading cause is that larger sinter particles contain more and larger closed pores and thus have greater porosity. Due to the larger bulk density of smaller particles, the packed bed using smaller particles has smaller porosity.

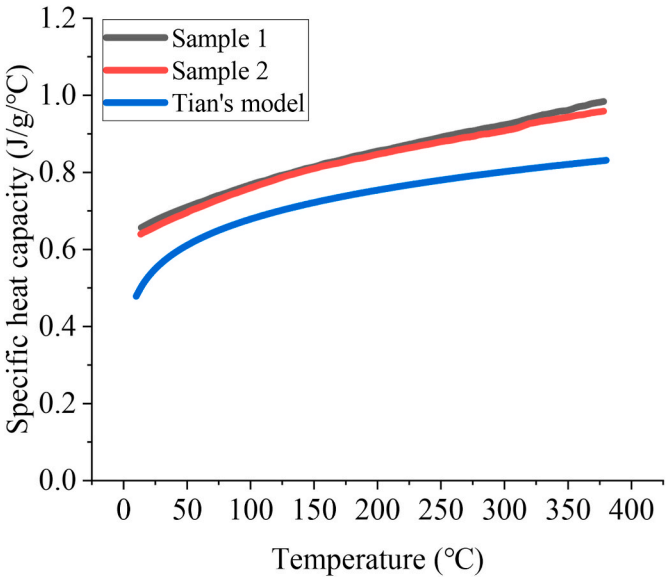

Fig. 2. Specific heat capacity of sinter as a function of temperature.

The specific heat of the sintered material was measured via a differential scanning calorimeter (TA Q200). The measurement temperature range was 0–400 °C, and the heating rate was 10 °C/min during the test. In the present work, the size of the sintered ore particle is 10–40 mm, which is too large to be put in the crucible of the differential scanning calorimeter. Therefore, the sintered ore particle was crushed into small particles of appropriate size before the specific heat was measured. To verify the reliability and repeatability of the experimental results, two samples randomly selected, 25.72 mg and 26.17 mg, were tested, respectively. Fig. 2 plots the specific heat of the two samples as a function of temperature. The specific heat of the sinter is 0.66–0.98 J/(g°C) in the range of 15–380 °C, which increases with the temperature rising. The results of the two samples are very close, indicating that the sampling is representative and the results are repeatable. For the convenience of comparison, the fitting curve of Tian's model [18] is shown, which is derived from the specific heat of the sinter measured via a differential scanning calorimeter. The trends of the specific heat are

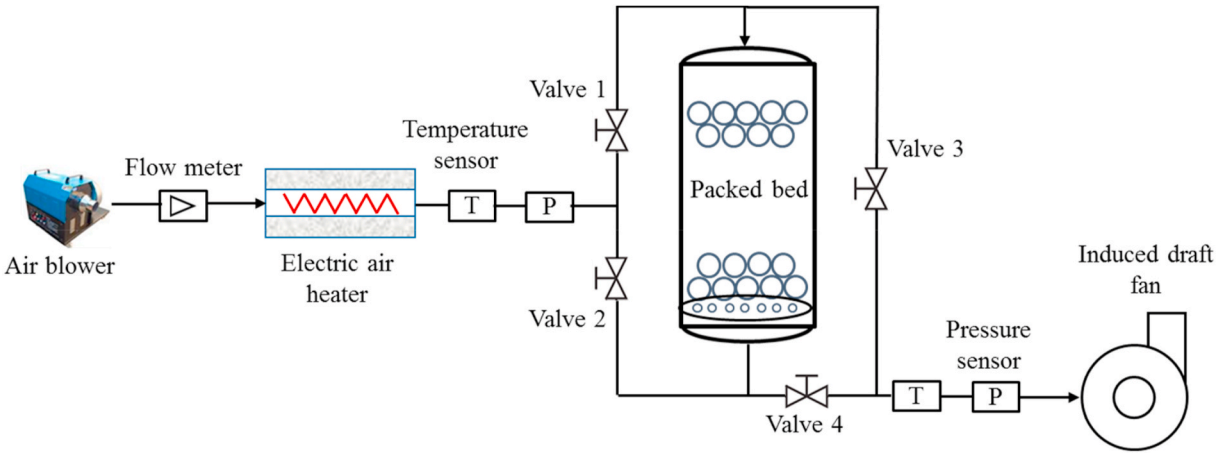

Fig. 3. Schematic diagram of the test system.

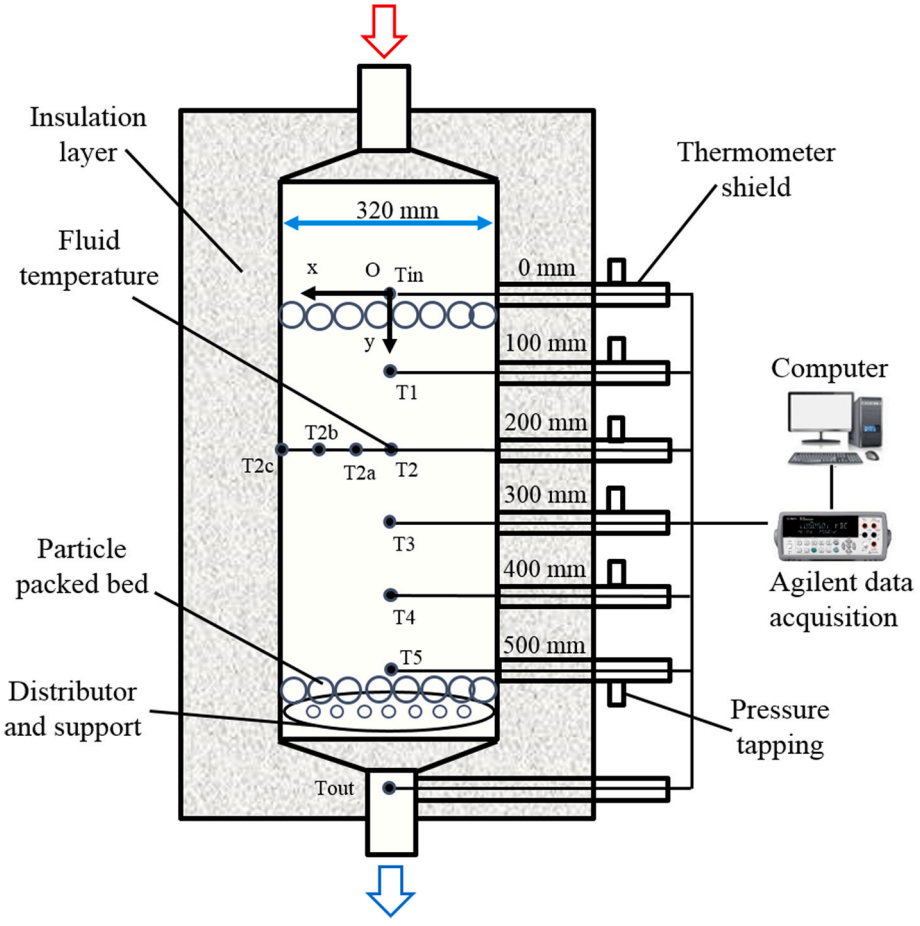

Fig. 4. Details of the storage tank and packed bed.

consistent with Tian' works, indicating that the current experimental results are reliable. The specific heat of the sintered ore particles is strongly affected by the composition of raw materials and sintering conditions. The differences in the two aspects primarily lead to the gap between our measurement results and those of Tian's work.

3. Experimental

3.1. Experimental system

Fig. 3 illustrates the schematic diagram of the experimental system. The system consists of a blower, electric air heater, storage tank and induced draft fan. Fig. 4 shows the details of the storage tank. The tank has an inner diameter of 320 mm and a height of 850 mm. The height of the sinter bed is 650 mm. For 25–40 mm, 16–25 mm and 10–16 mm particles, the average particle diameter is 32 mm, 20 mm and 13 mm,

Table 2
Experimental conditions and results of storage performances of sinter bed.

Case	Particle size (mm)	T' (°C)	V (m^3/h)	$\eta_{charging}$ (%)	$\eta_{discharging}$ (%)	η_{cycle} (%)
1	25–40	300	85	61.34	68.92	42.28
2	16–25	300	85	62.55	70.47	44.08
3	10–16	300	85	63.26	71.33	45.12
4	10–16	250	85	62.91	71.40	44.92
5	10–16	200	85	64.17	71.54	45.90
6	10–16	200	130	68.45	80.99	55.44
7	10–16	200	175 (1st)	70.08	82.19	57.60
8	10–16	200	175 (2nd)	63.53	102.03	64.82
9	10–16	200	175 (3rd)	63.13	105.77	66.78

respectively. Therefore, for all sizes of particles, the ratio of tank diameter to particle diameter is greater than or equal to 10, so the edge effect was small [32,33].

The tank is made of 310S stainless steel with a wall thickness of 10 mm. To reduce heat loss, a 250 mm castable insulation layer was arranged around the tank, and a 150 mm insulation layer was arranged in the piping system.

3.2. Experimental procedure

For the cold tests, ventilate the bed to study the effect of particle size on the airflow resistance characteristics of the bed. The tests of the air resistance characteristics were conducted in a cold state at an ambient temperature of about 20 °C. During the tests, the blower remained closed, and the induced draft fan provided the airflow. The air flow was controlled by setting the negative pressure of the pipeline and the valve opening of the induced draft fan with a rated fan power of 90 kW.

For the thermal tests, the induced draft fan was turned off. During charging, the air provided by the blower flowed through the electric heater and was heated to a predetermined temperature. Then the heated hot air passed through the storage tank longitudinally from top to bottom while transferring heat to the sinter bed. Finally, the air from the storage tank was discharged into the atmosphere. When the outlet air temperature of the tank reached 0.65 times the predetermined temperature $\theta = \frac{T_{out}}{T'} = 0.65$, the charging stopped. During discharging, the electric heater was closed, and the low-temperature air from the blower passed through the storage tank from the bottom to top, and was heated by the bed and then was discharged into the atmosphere. From the perspective of energy grade, the air below 60 °C is not useful even if used for space heating. Therefore, the discharging stopped when the outflow temperature dropped below 60 °C. It is worth mentioning that before each test, ventilate the bed in a cold state until the bed temperature is close to room temperature to eliminate the influence of residual heat in the bed on the experimental results. Besides, to protect the electric heater, it must be cooled to below 60 °C before discharging. Therefore, there was an about 20–40 min cooling process between the charging and discharging. During the tests, the air flow rate was controlled by adjusting the blower valves with a rated fan power of 0.55 kW. The inlet air temperature was adjusted by setting the temperature (heating program) of the electric heater with a maximum heating power of 90 kW. Table 2 gives the test cases of the hot state tests.

3.3. Data collection

As shown in Fig. 4, five thermocouples were arranged at intervals of 100 mm to measure the axial temperature in the bed. Another two thermocouples were arranged at the top and bottom of the bed to measure the air temperature at the inlet and outlet of the tank. Other thermocouples were used to measure radial temperature distributions. All temperatures were detected by K-type thermocouples with ±1.5 °C accuracy, and Agilent was used for data collection. The data sampling interval was 10 s. The pressure sensors were used to measure the air flow pressure drop through the bed layer by the pressure tappings. The data sampling interval was 1 s, and the sampling accuracy was 1 Pa. The air velocity/flow rate was measured by the Testo 435 micro-manometer, the data sampling interval was 1 s, and the sampling accuracy was 0.1 m/s.

3.4. Data reduction

In terms of studying airflow resistance characteristics, the Japanese were the first to use a small cylindrical air permeability device to simulate the packing arrangement of sinter materials and study the sinter bed permeability. Due to the wide acceptance and use of Japanese Permeability Units (JPU) in sintering, and considering that sinter particles are also used as the packed bed storage material in this work, the author innovatively proposes to introduce JPU into the field of packed bed energy storage. In the current work, JPU is used as a quantitative index to characterize the airflow resistance characteristics of packed beds [34].

$$JPU = \frac{V}{60S}\left(\frac{H}{\Delta P}\right)^{0.6} \tag{3}$$

The air flow can be calculated by the following equation:

$$V = S_{pipe} \times v_{pipe} \tag{4}$$

The mass flow rate of air can be calculated by the following equation:

$$m = V \times \rho_{air} \tag{5}$$

During charging, the instantaneous amount of energy stored in the packed bed can be obtained by the following equation [35]:

$$Q_{stored} = mc_{pair} \cdot \Delta t(T_{in} - T_{out}) \tag{6}$$

The input energy during charging can be calculated by the following equation [10]:

$$E_{input} = \int_{t_o}^{t_{end}} \int_{T_o}^{T_{end}} m \cdot c_{pair} dT \cdot dt \tag{7}$$

The pumping energy during charging or discharging can be obtained by the following equation [10]:

$$E_{pump} = \int_{t_o}^{t_{end}} V \Delta p dt \tag{8}$$

During discharging, the instantaneous amount of energy released from the packed bed can be obtained by the following equation [35]:

$$Q_{release} = mc_{pair} \cdot \Delta t \cdot (T_{out} - T_{in}) \tag{9}$$

Charging efficiency [35], discharging efficiency and cycle efficiency are introduced [10] to evaluate the thermal performance of sinter as energy storage materials. Charging efficiency is the ratio of the total energy stored in the tank to the sum of the total energy input and the pump work during charging.

$$\eta_{charging} = \frac{\int_{t_o}^{t_{end}} Q_{stored} \cdot dt}{E_{input} + E_{pump}} = \frac{\int_{t_o}^{t_{end}} mc_{pair}(T_{in} - T_{out}) dt}{\int_{t_o}^{t_{end}} \int_{T_o}^{T_{end}} mc_{pair} dT dt + \int_{t_o}^{t_{end}} V \Delta p dt} \tag{10}$$

Discharging efficiency is the ratio of the total energy released from the tank to the sum of the stored heat and the pump work during discharging.

Table 3
Experimental uncertainties of the major parameters of interest.

Property/parameter (unit)	Symbol	Uncertainty (%)
Air flow (m^3/h)	V	1.46
Pressure drop per unit length (Pa/m)	Δp/H	1.15
Reduced pressure drop (Pa·s/m^2)	Δp/HU	1.87
Permeability	JPU	1.64
Energy stored (kWh)	–	1.61
Energy released (kWh)	–	1.90
Charging efficiency (%)	$\eta_{charging}$	2.28
Discharging efficiency (%)	$\eta_{discharging}$	2.49
Cycle efficiency (%)	η_{cycle}	2.50

$$\eta_{discharging}=\frac{\int_{t_o'}^{t_{end}'} Q_{release}\cdot dt}{\int_{t_o'}^{t_{end}'} Q_{stored}\cdot dt+E_{pump}}=\frac{\int_{t_o'}^{t_{end}'} mc_{pair}(T_{out}-T_{in})dt}{\int_{t_o'}^{t_{end}'} mc_{pair}(T_{in}-T_{out})dt+\int_{t_o'}^{t_{end}'} V\Delta p dt} \tag{11}$$

Cycle efficiency is defined as the ratio of the heat released to the sum of the input energy and the required pump work in a complete charging/discharging cycle.

$$\eta_{cycle}=\frac{\int_{t_o'}^{t_{end}'} Q_{release}\cdot dt}{E_{input}+E_{pump(charging)}+E_{pump(discharging)}}=\frac{\int_{t_o'}^{t_{end}'} mc_{pair}\Delta t(T_{out}-T_{in})dt}{\int_{t_o}^{t_{end}}\int_{T_o}^{T_{end}} m\cdot c_{pair}dT\cdot dt+\int_{t_o}^{t_{end}} V\Delta p dt+\int_{t_o'}^{t_{end}'} V\Delta p dt} \tag{12}$$

The non-dimensional index stratification number (Str) is used to quantitatively evaluate the thermal stratification performance of the sinter bed [36,37]. Str is defined as the ratio of the average value of the temperature gradient at any time t to the maximum average temperature gradient during charging/discharging.

$$Str=\frac{\overline{\left(\frac{\partial T}{\partial y}\right)_t}}{\left(\frac{\partial T}{\partial y}\right)_{max}}=\frac{\frac{1}{I-1}\cdot\left[\sum_{i=1}^{I-1}\left(\frac{T_{i+1}-T_i}{\Delta y}\right)\right]}{\frac{T_{in}-T_{inj}}{(I-1)\cdot\Delta y}} \tag{13}$$

Additionally, the major parameters' maximum uncertainty was evaluated via the error propagation theory [38], as given in Table 3.

$$\delta R=\left[\sum_{i=1}^{N}\left(\frac{\partial R}{\partial X_i}\delta X_i\right)^2\right]^{1/2} \tag{14}$$

Where δR is the total uncertainty, X_i is the measurement parameter, δX_i is the uncertainty of each independent variable, which can be calculated according to the accuracy of measuring instruments and measured values.

4. Results and discussion

4.1. Air resistance characteristics of packed bed

4.1.1. Cold air resistance characteristics

Fig. 5(a) shows the ΔP/H of the packed bed of sintered ore particles with different nominal sizes under different air superficial velocities. ΔP/H increases with the air superficial velocity rising, and the overall trend of the curve fits well with the binomial [39,40]. At the same air superficial velocity, the smaller the particle size, the greater the ΔP/H

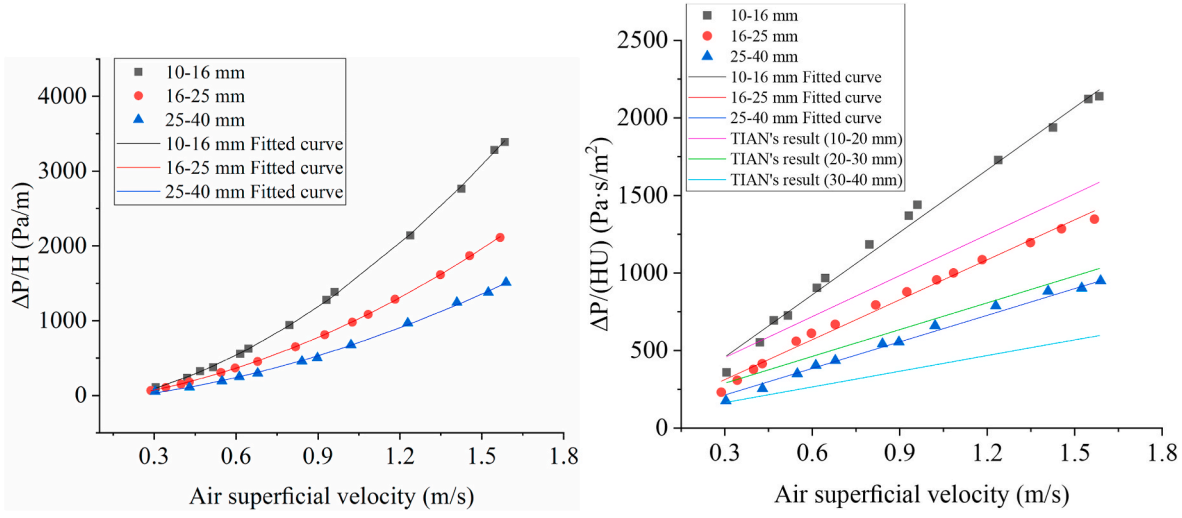

(a) ΔP/H (b) ΔP/(HU)

Fig. 5. Effect of U on ΔP/H and ΔP/(HU) for different particle sizes.

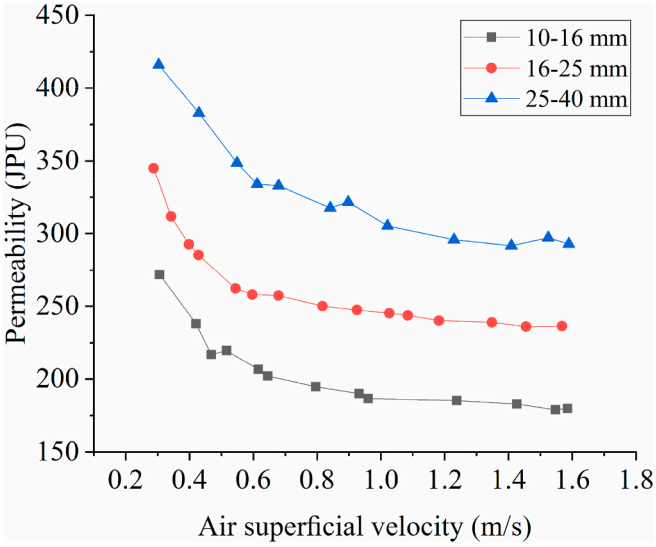

Fig. 6. Effect of U on bed permeability for different particle sizes.

and thus the more significant the airflow resistance. Fig. 5(b) shows the reduced pressure drop [30] of the packed bed of sintered ore particles with different nominal sizes under different air superficial velocities. The reduced pressure drop of the bed increases as the air superficial velocity increases, and the overall trend of the curve conforms to the linear law [30,31]. At the same air superficial velocity, smaller particles cause more significant reduced pressure drops and thus greater airflow resistance.

The results of Tian's test [30] for sintered ore particles have been added to Fig. 5(b) for comparison. The variation trends of the ΔP/(HU) with particle size are consistent with Tian's works, indicating that the current experimental results are accurate and reliable. On this basis, the bed permeability index JPU is innovatively introduced to characterize the airflow resistance characteristics of the bed. Fig. 6 plots the bed permeability at different air superficial velocities under three particle sizes. The bed permeability first decreases and then gradually approaches a stable value as the air superficial velocity increases. Furthermore, the bed permeability decreases as the particle size decreases. According to Ergon's equation, the permeability of the packed bed is mainly affected by the average particle diameter and the voidage of the packed bed. Particles in the smaller nominal size range result in smaller average particle sizes and a smaller bed voidage, leading to worse bed permeability, namely, more significant airflow resistance. In summary, at the same air superficial velocity, the permeability index JPU can characterize the airflow resistance of the sinter bed well.

4.1.2. Thermal air resistance characteristics

Taking case 6 as an example, Fig. 7 shows the airflow resistance characteristics during the thermal tests. In the current tests, the fan power and the valve opening in the pipeline remain unchanged. The air flow declines slowly and slightly during charging and rises slowly and slightly during discharging. The pressure drop of the air through the beds can be calculated using the Ergun equation, which has been modified with a buoyancy term [9]:

$$\frac{\Delta p}{H}=\frac{G^2}{\rho_{air}d}\left(A\frac{(1-\varepsilon)}{\varepsilon^3\Phi^2}\frac{\mu}{Gd}+B\frac{1-\varepsilon}{\varepsilon^3\Phi}\right)+\rho_{air}g\frac{\Delta T}{T} \tag{15}$$

For equation (15), the first and second terms in the parentheses are viscous and kinetic energy losses, respectively. The second term takes into account the pressure difference over the bed layer caused by temperature difference. It has an augmenting effect on the pressure drop during charging and a reducing effect during discharging. During charging, the overall temperature inside the bed rises, causing the density to decrease and the dynamic viscosity to increase, which in turn increases the pressure drop according to Eq. (15). However, the power of the air blower remains constant. Therefore, the air flow declines slowly and slightly during charging. Similarly, the opposite is true during discharging [5,9].

4.2. Thermal behavior of sinter bed

Taking case 3 as an example, Fig. 8 shows the axial temperature evolution over time during charging and discharging. For charging, the axial temperature gradually climbs with time in sequence. At the beginning of charging, the inlet air temperature soars to close to the predetermined temperature, while the bed temperature remains the ambient temperature. Due to the significant temperature difference, the heat transfer between the heat transfer fluid and the storage material is intense, so the bed temperature rises rapidly. As the charging progresses, the temperature difference between the inlet air temperature and the bed temperature gradually decreases, so the heat transfer becomes gentle and thus the bed temperature rises slowly. It is worth pointing out

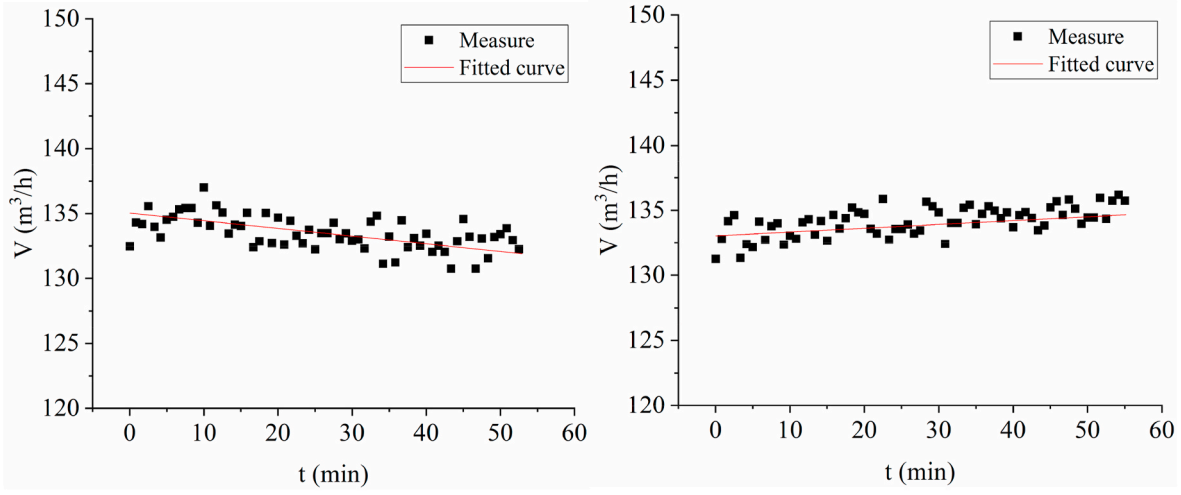

Fig. 7. The evolution of air flow during charging and discharging.

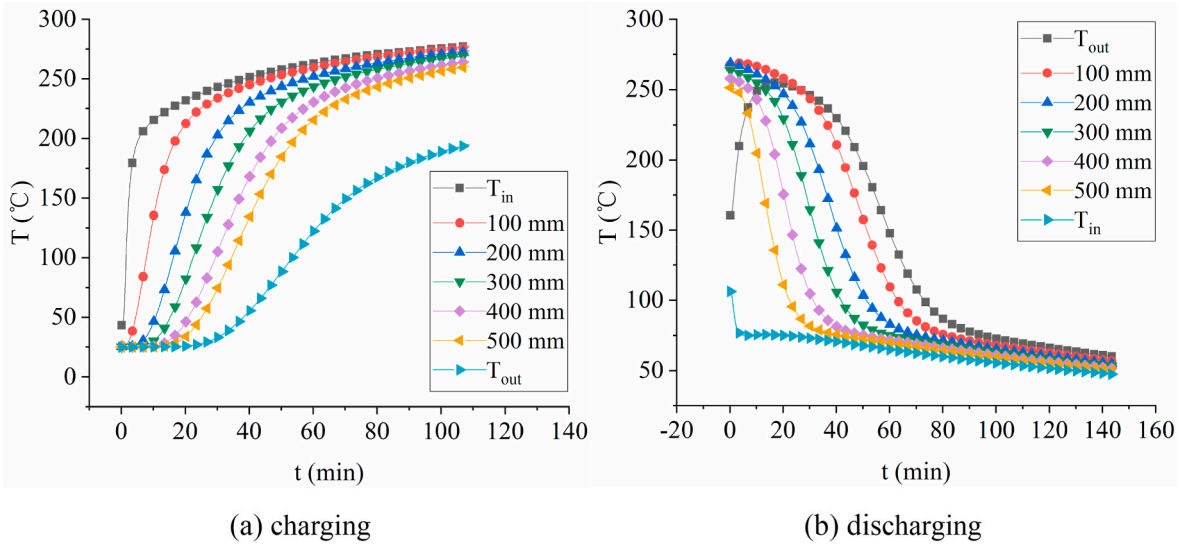

Fig. 8. Axial temperature profile during charging and discharging.

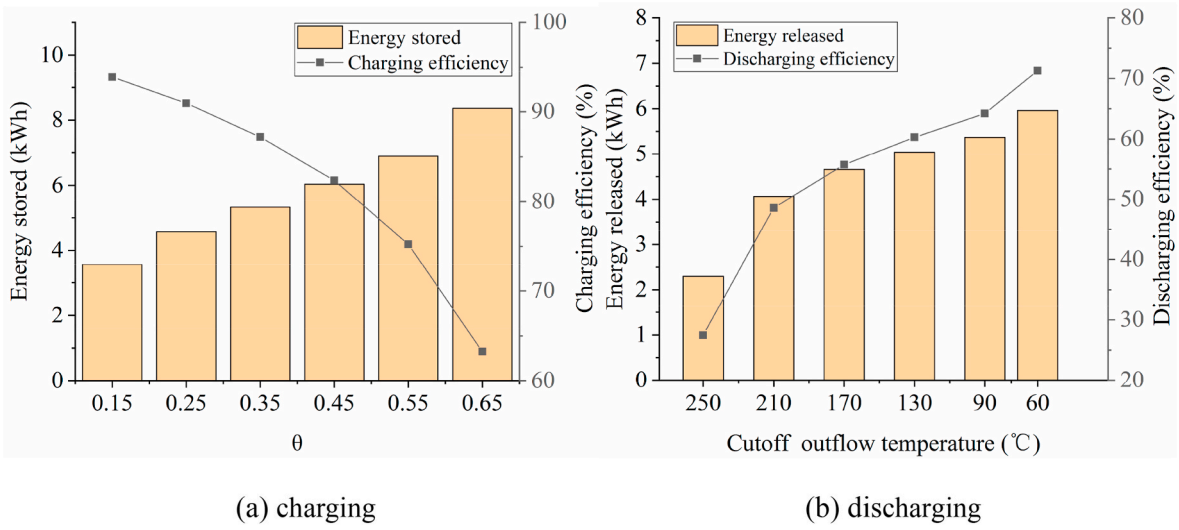

Fig. 9. Effect of cutoff outflow temperature on thermal performance.

that the thermal behavior in the bed is not transversely uniform due to radial heat dissipation in the present test. This result indicates that the current axial temperature only represents the temperature along the central axis of the tank and does not represent the average temperature of the bed cross-section. In this study, the axial temperatures are only used to analyze the movement and thermal behavior of the heat transfer front inside the bed, but not to calculate the storage capacity of solid material. The same is below. Given that the size of this manuscript, the influence of different parameters on the radial temperature uniformity of the bed will be discussed in the next manuscript.

It is worth noting that the temperature difference between the 500 mm position and the exit is about 60 °Cat the end of charging. This temperature difference is explained for the following reasons. First, the total height of the bed is 650 mm, which means that there is still a 150 mm bed under the thermocouple at 500 mm to absorb heat. Second, the temperature measured by the thermocouple at 500 mm is the temperature at the center of the bed. Due to the radial heat dissipation, the temperature near the wall is significantly lower than the temperature at the center. The low-temperature airflow near the wall and the high-temperature airflow at the center of the bed converge at the tank's outlet, so it is not difficult to understand that the temperature at the outlet of the tank is much lower than the bed temperature at 500 mm. Besides, since the pipeline at the bottom of the storage tank cannot be preheated during the pipeline preheating process, the airflow is cooled by the tank's base after it flows out from the bottom of the tank.

For discharging, the axial temperature gradually declines with time in sequence. The thermal behavior of the bed is similar to that during charging, but the curve change trend is opposite.

Fig. 9(a) shows the heat stored and charging efficiency at different dimensionless cut-off temperatures during charging. When the dimensionless cut-off outflow temperature increases from 0.15 to 0.65, the heat stored increases from 3.56 kWh to 8.36 kWh while the corresponding charging efficiency drops from 93.9% to 63.3%. Charging deeper for storing more heat will inevitably decrease charging efficiency and thus cycle efficiency. This result means that the charging efficiency and the total energy stored are a pair of contradictions. A compromise must be made from a technical and economic perspective. Fig. 9(b) shows the heat released and discharging efficiency at different cut-off outflow temperatures during discharging. When the cut-off outflow temperature gradually reduces from 250 °C to 60 °C, the heat released gradually increases from 2.30 kWh to 5.96 kWh, and the discharging efficiency also gradually increases from 27.5% to 71.3%.

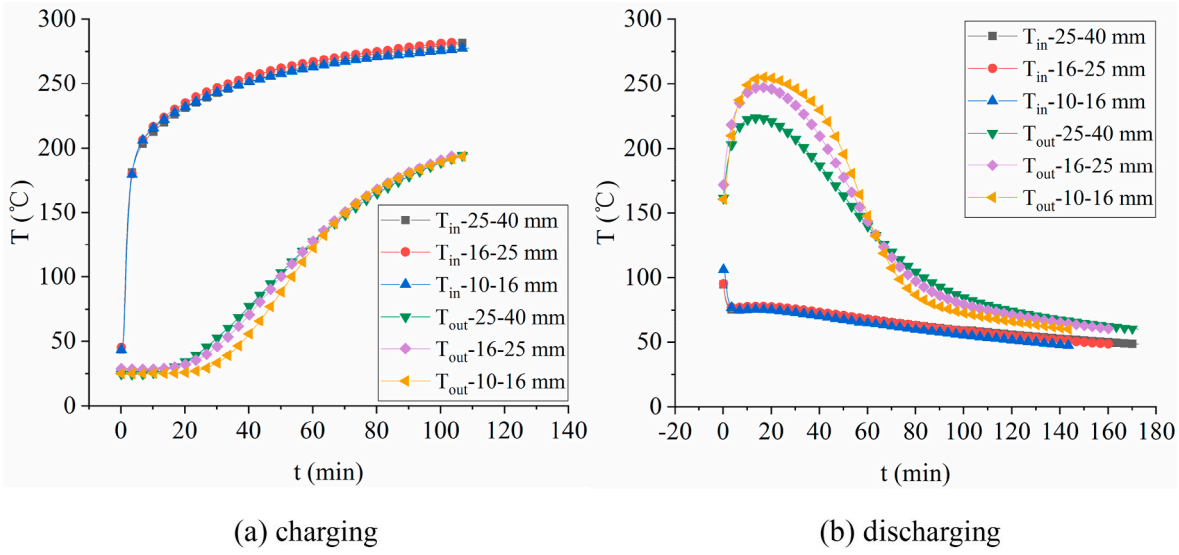

Fig. 10. Effect of particle size on inlet and outlet temperature during charging and discharging.

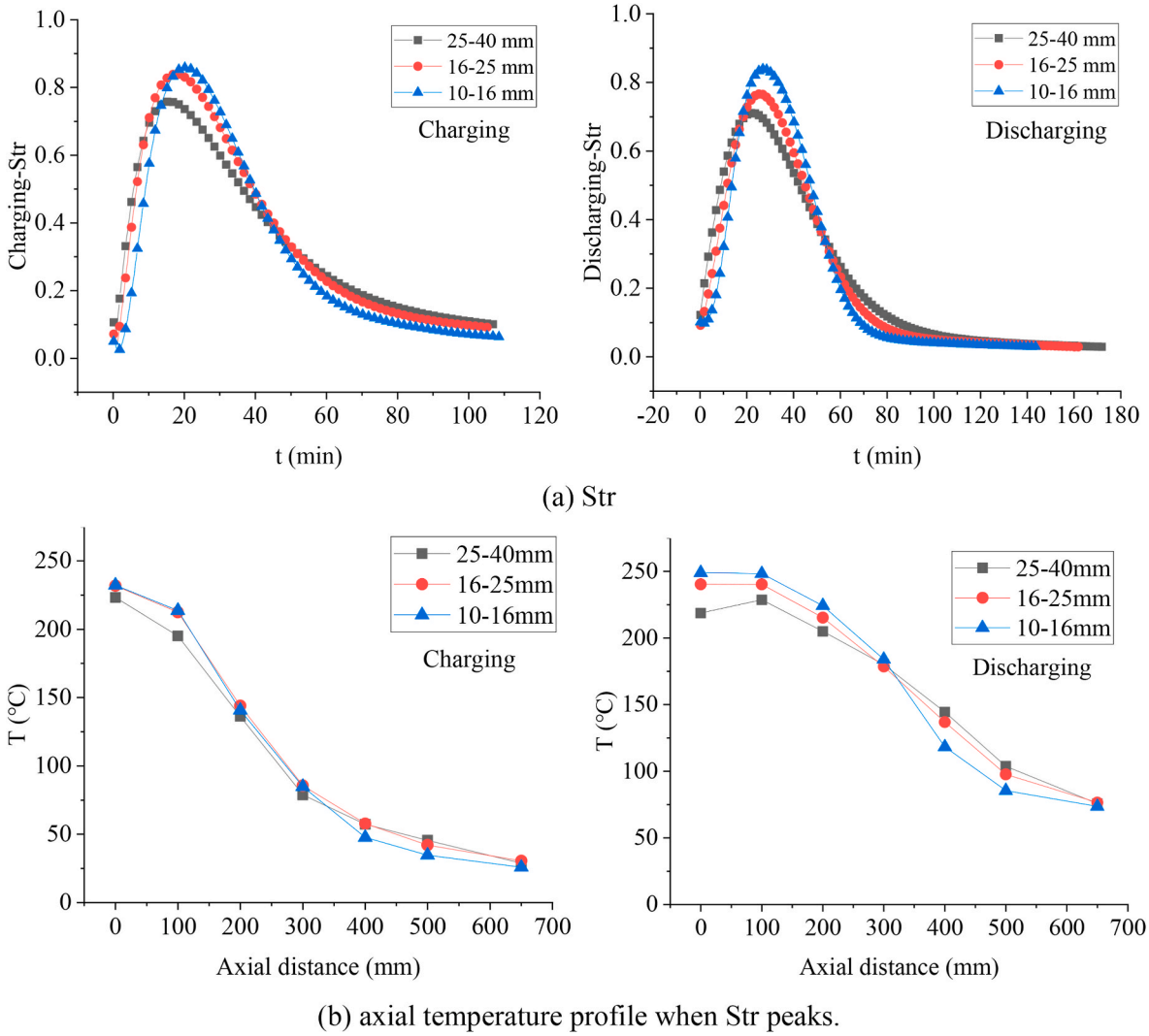

Fig. 11. Effect of particle size on thermal stratification.

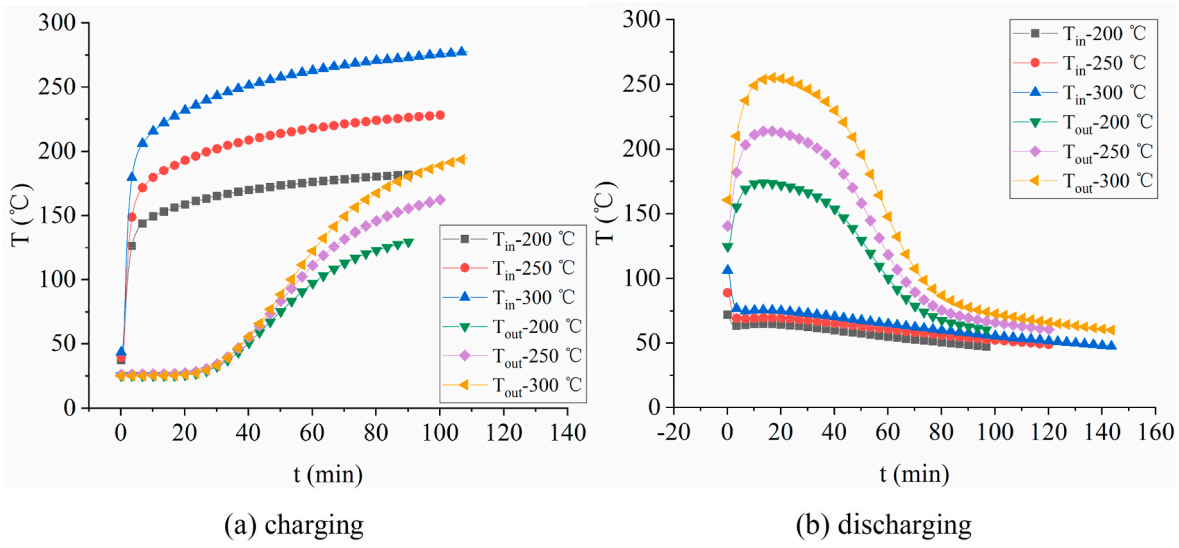

Fig. 12. Effect of charging temperature on inlet and outlet temperature during charging and discharging.

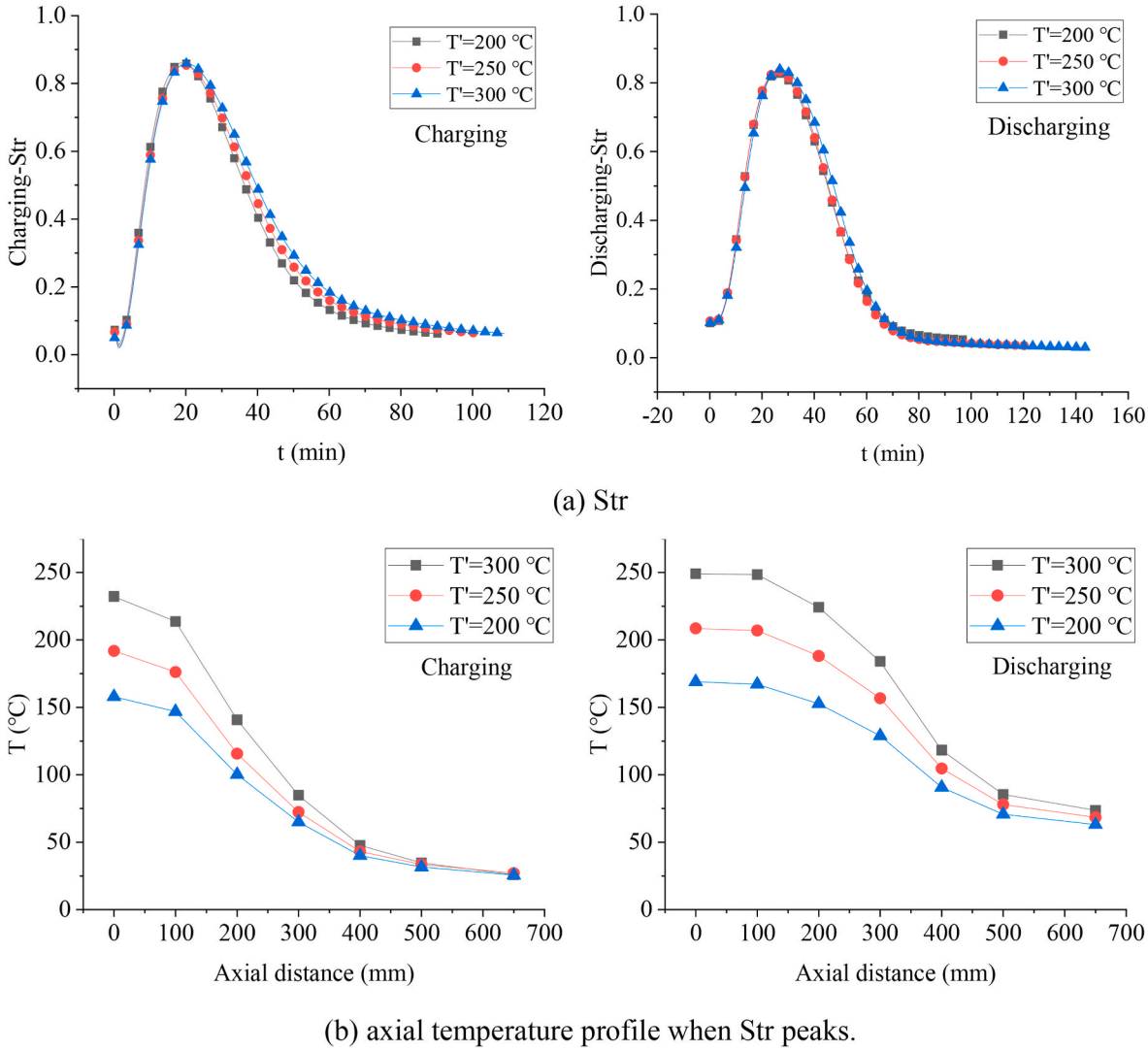

Fig. 13. Effect of charging temperature on thermal stratification.

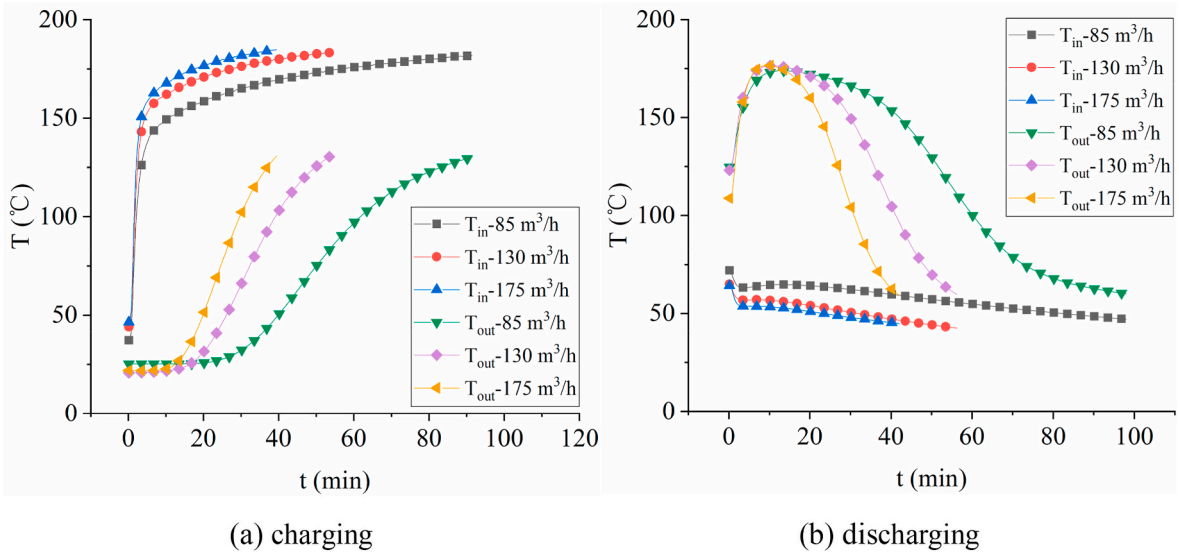

Fig. 14. Effect of air flow on inlet and outlet temperature during charging and discharging.

Table 2 shows the experimental results of storage performances of the sinter bed. For the current case, cycle efficiency is 45.12%. The following two reasons can explain the low cycle efficiency. First, the dimensionless outlet temperature reaches 0.65 during charging, which is a deep charging process. As illustrated in Fig. 9(a), the deeper charging, the more heat loss, and thus the lower the charging efficiency. In the late stage of charging, as the outlet temperature gradually rises, the heat loss increases rapidly. Second, the current test is a single charging/discharging cycle test, and the sign of the end of the discharging is that the outlet temperature drops below 60 °C. This operation procedure means that part of the heat remains in the tank after discharging. When multiple continuous cycle tests are carried out, the residual heat in the tank at the end of the last cycle can be used in the next cycle so that a higher cycle efficiency can be obtained.

4.3. *Effect of particle size on thermal performance*

Fig. 10 shows the effect of sinter particle size on inlet and outlet temperature. The larger the particle size, the earlier the outlet air temperature rises. This result is because the specific surface area is more significant for smaller particles, and the voidage of the packed bed formed by the smaller particle is lower, thus a larger heat exchange area. These factors lead to better heat exchange between the storage material and the heat transfer fluid [36], which ultimately reduces heat diffusion from the top to the bottom of the bed. For the discharging process, when the particle size gradually decreases, the curve of outlet air temperature gradually becomes higher and narrower. This change means that the heat release of smaller particles is more concentrated; hence, smaller particles have a higher peak outlet temperature and a shorter discharging time. A packed bed of small particles is easier to produce and maintain a sharp thermocline [10] during heat exchange. Besides, the actual flow velocity in the bed is greater for small particles. These factors ultimately lead to greater heat transfer power.

Fig. 11 shows the effect of particle size on thermal stratification. Thereinto, Fig. 11(a) shows the evolution of Str, and Fig. 11(b) shows the axial temperature profiles in the tank when Str reaches its peak (the same below). Regardless of the charging or discharging, the Str first increases and then decreases, indicating the formation and recession of thermal stratification in the bed. Small particle materials have higher peak Str [10], and the peaks appear later. Meanwhile, Fig. 11(b) indicates that the thermocline of the bed with smaller particles is sharper and steeper. As mentioned above, the bed with smaller particles has a larger heat transfer area and a smaller bed voidage, which hinders the heat diffusion from the inlet to the outlet of the tank [36] and promotes the formation and maintenance of thermocline in the tank.

The effect of particle size on storage performances can be seen in Table 2. For small particles, the packed bed has a smaller voidage, which means a greater mass of storage materials and more heat stored. Furthermore, the packed bed of small particles loses less heat during the cycle process, and finally 10–16 mm particle has the highest cycle efficiency [10].

4.4. *Effect of charging temperature on thermal performance*

Fig. 12 shows the effect of charging temperature on inlet and outlet temperature. The higher the charging temperature, the greater the slope of the outlet temperature curve. This result is because the higher the charging temperature, the more significant the temperature difference between the heat transfer fluid and the bed, and thus the greater the heat transfer *Nu* number [1]. However, as the charging temperature increases, the corresponding charging time is also prolonged. When the charging temperature increases from 200 °C to 250 °C, 300 °C, the charging time increases from 91.5 min to 100.7 min and 108.8 min, respectively. A higher charging temperature also causes a higher outlet temperature during discharging. When the charging temperatures are 200 °C, 250 °C, and 300 °C, the corresponding peak outflow temperatures are 173.9 °C, 213.9 °C, and 255.0 °C, respectively.

Fig. 13 shows the effect of charging temperature on thermal stratification. The curves of Str evolution with time at different charging temperatures almost overlap, indicating that the charging temperature has little effect on the thermocline velocity. Higher charging temperatures increase heat transfer temperature differences, resulting in a steeper thermocline, as shown in Fig. 13(b). However, the charging temperature has less impact on the peak value of Str shown in Fig. 13(a). According to the definition of the Str, a higher charging temperature leads to an increase of the average temperature gradient, while the maximum average temperature gradient as the denominator also increases, so the Str is almost unchanged.

The effect of charging temperature on storage performances is shown in Table 2. Within the temperature range of current tests, the charging efficiency, discharging efficiency, and cycle efficiency have no apparent changing trend with the change of charging temperature. A higher charging temperature leads to an increase in heat loss, while the total amount of stored heat also increases, and eventually the proportion of heat loss does not change much [8].

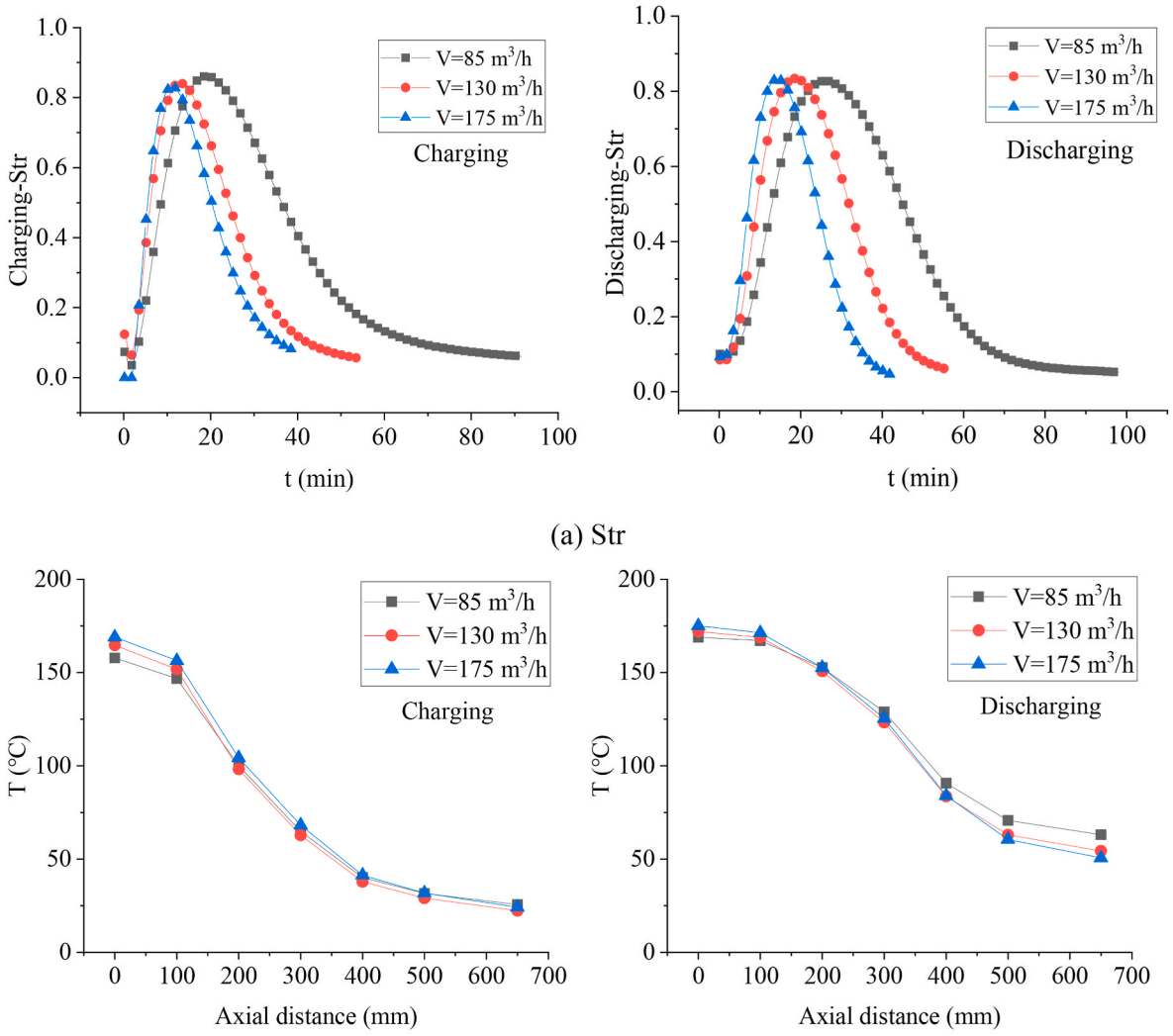

Fig. 15. Effect of air flow on thermal stratification.

4.5. *Effect of air flow on thermal performance*

Fig. 14 shows the effect of air flow on inlet and outlet temperature. The greater the air flow, the earlier the outlet temperature rises, and the greater the curve slope. The greater the air flow, the greater the superficial velocity of the heat transfer fluid passing through the storage tank. When the air flow gradually increases from 85 m^3/h to 130 m^3/h, 175 m^3/h, the air superficial velocity in the tank also gradually increases from 0.3 m/s to 0.45 m/s and 0.6 m/s, respectively. The increase of the airflow velocity leads to a rise in the heat transfer *Nu* number between the air and the bed material [1], so the heat carried by the heat transfer fluid can be transferred to the storage material faster. When the air flows are 85 m^3/h, 130 m^3/h, and 175 m^3/h, the charging times are 91.5 min, 54.2 min and 39.5 min, respectively. Due to the larger heat transfer coefficient caused by the larger flow rate, the 175 m^3/h case has the highest peak outlet temperature of 176.58 °C during discharging. When the air flow gradually increases, the discharging curve gradually becomes narrower and taller, which means the heat release is more concentrated. When the air flows are 85 m^3/h, 130 m^3/h, and 175 m^3/h, the discharging times are 98.0 min, 56.3 min and 42.0 min, respectively.

Fig. 15 shows the effect of air flow on thermal stratification. With the increase of the air flow, the evolution curve of the Str gradually becomes narrower and the peak comes earlier due to the faster charging and discharging processes. Meanwhile, the air flow has little effect on Str peak value. The speed of the thermocline through the beds depends on the air velocity, which is directly proportional to the used thermal power [12]. As the air flow increases, the air velocity increases, driving the thermocline to move faster. In addition, when the charging temperature remains constant, the greater the air flow, the greater the charging power, thus enhancing the heat transfer. These factors accelerate the charging process, so the time required to obtain maximum Str decreases with increasing air flow rate. The same is valid for discharging.

From Fig. 15(b), the thermocline becomes slightly steeper as the air flow increases. However, when the air flow increases from 85 m^3/h to 130 m^3/h and 175 m^3/h, the peak charging Str decreases from 0.861 to 0.841 and 0.831, respectively. This contradiction arises from the definition of Str. For the three different air flow cases, when the thermal gradients in the bed reach the peak, the inlet air temperatures are not wholly consistent but with tiny differences. This difference leads to a difference in the denominator in Str, which leads to a situation where Str results are inconsistent with thermal gradient results.

In fact, greater air flow has a twofold effect on the thermocline within the bed. On the one hand, when the air flow increases, the heat transfer coefficient increases, making the thermocline even sharper [12]. On the other hand, as the air flow rises, the residence time of the heat transfer fluid in the bed decreases, which makes the heat transfer fluid still has residual heat to heat the bottom particles after passing through the top particles. Therefore, the heat transfer fluid at a large

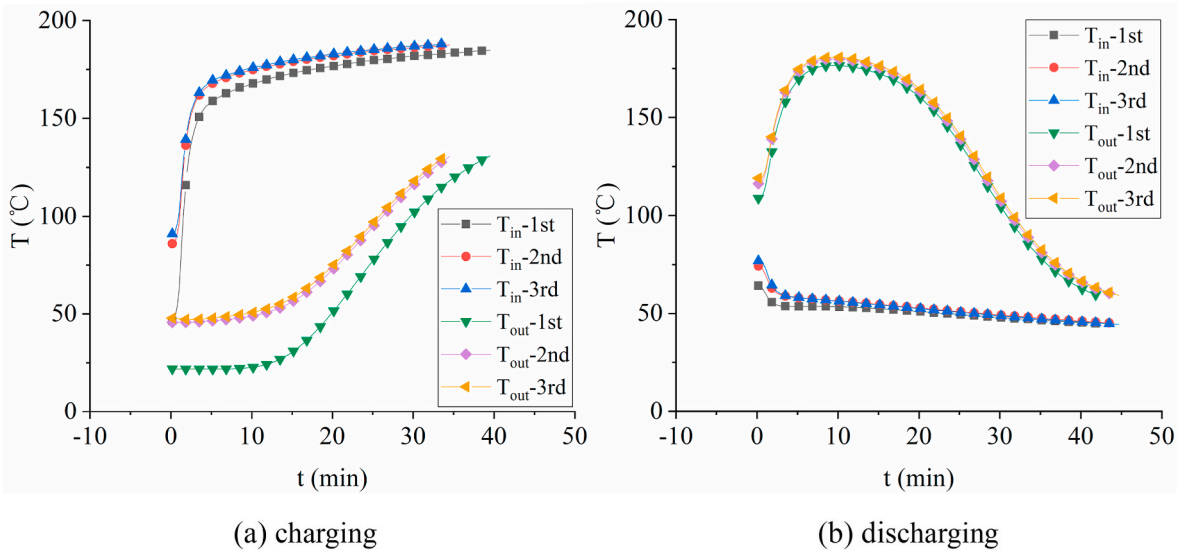

Fig. 16. Effect of cycle times on inlet and outlet temperature during charging and discharging.

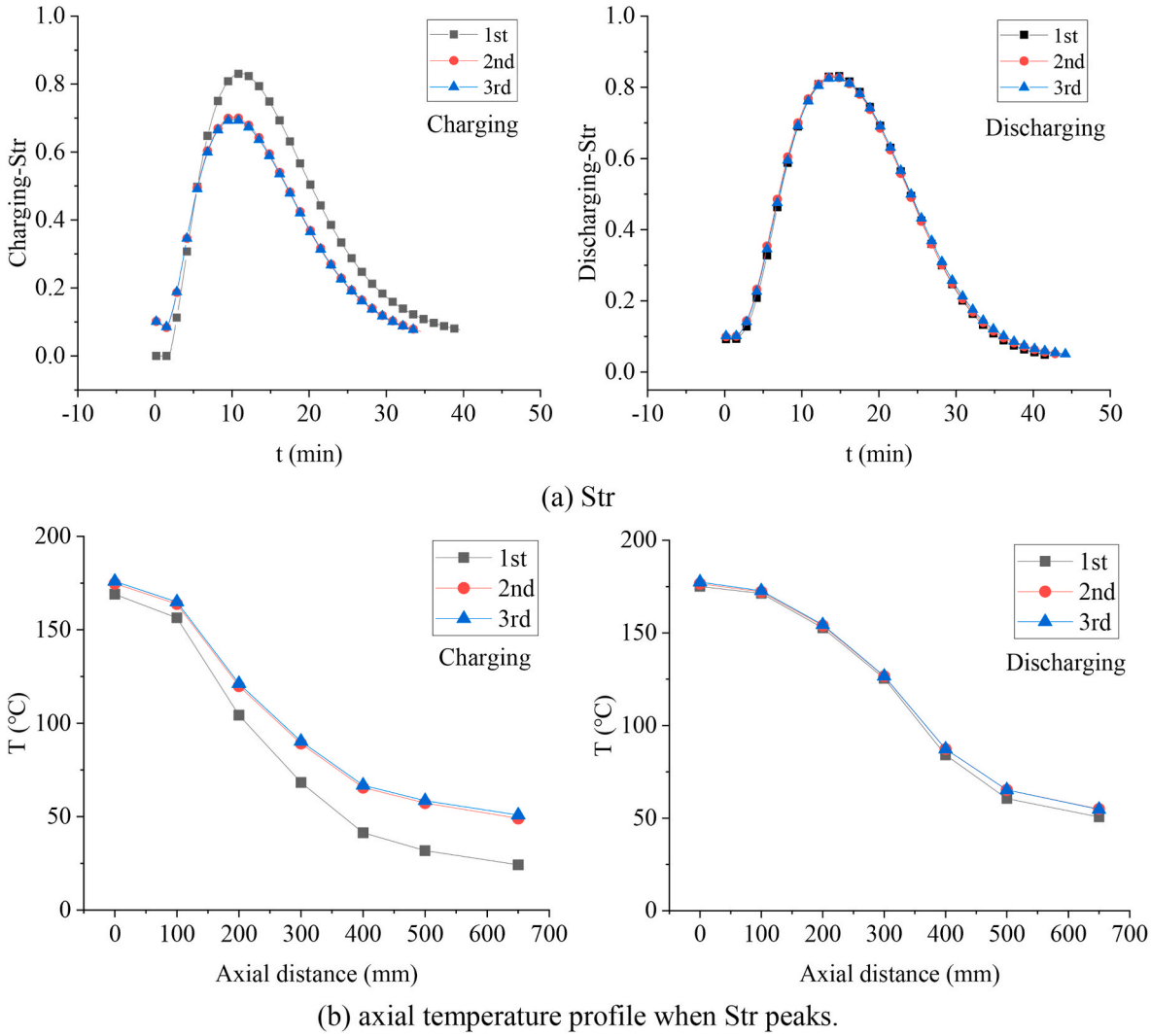

Fig. 17. Effect of cycle times on thermal stratification.

flow rate tends to heat the particles more uniformly in the axial direction, while at a small flow rate, the heat transfer fluid tends to heat the particles near the inlet first [11,37]. In addition, higher flow rates may result in more chaotic flow within the bed, which may disturb the formation and development of thermocline [26]. The final thermocline of the bed depends on the combined effect of these factors.

The effect of air flow on storage performances can be seen in Table 2. Larger air flow leads to more considerable heat transfer power and shorter process time, so the system's heat loss is less [26]. As air flow increases, the charging efficiency and discharging efficiency both rise, and thus finally the cycle efficiency also rises. In addition, since the discharging is carried out after the electric heater is cooled to below 60 °C, the larger flow rate results in a slightly lower average inlet air temperature during discharging, as shown in Fig. 14, which also increases the discharging efficiency and cycle efficiency to a certain extent.

4.6. Cycle performance of storage tank

The above tests are all single charging/discharging cycle tests, but the system runs continuously and carries out multiple charging/discharging cycles in actual applications. During the continuous storage cycles, since the charging is carried out in the thermal state after the last discharging, the system often exhibits storage characteristics different from those of the single cycle. This part focuses on comparing the energy storage characteristics of the single-cycle test and multiple-cycle test.

Fig. 16 shows the evolution of the air temperature at the inlet and outlet of the tank over time during the three charging/discharging cycles. Due to the preheating effect of the first cycle on the system, the inlet air temperature rises faster in the second and third cycles and is slightly higher than that in the first cycle. In addition, the initial outlet temperature is higher, and the charging time is shorter in the second and third cycles than those in the first cycle due to incomplete heat release in the last cycle. The difference in discharging among the three cycles is negligible. Because of the better preheating effect provided by the long run of the system, the temperature curves in the latter two cycles are slightly higher than that in the first cycle.

Fig. 17 shows the evolution of thermal stratification over time in the three cycles. As shown in Fig. 17(b), the charging thermoclines of the latter two cycles are much flatter than that of the first due to the smaller temperature difference caused by the higher initial bed temperature. The peak Str decreases from 0.831 in the first cycle to 0.702 and 0.696, respectively. The discharging Str curves in the three cycles almost overlap, indicating that cycle times have little effect on the discharging thermal stratification characteristics.

The storage performances in three cycles are shown in Table 2. Due to the incomplete heat release in the first cycle, the heat stored in the subsequent cycles is significantly less than that in the first cycle, and thus the charging efficiency decreases. Since the long-run system is more fully preheated, the heat released and the discharging efficiency gradually increase with the number of cycles. It is worth noting that the discharging efficiency slightly exceeds 100% in the latter two cycles because the energy progressively accumulated in the experimental system in the previous cycles is released in the subsequent cycles. In general, the cycle efficiency increases as the number of cycle increases. Due to the incomplete heat release, the cycle efficiency in the first cycle is significantly lower than that in subsequent cycles. After the first cycle, the continuously running system gradually enters a stable state, and the cycle efficiency is slightly improved.

5. Conclusions

This paper proposes using sintered ore particles as a sensible heat storage material and experimentally studies the airflow resistance and energy storage characteristics of the sinter bed. The main conclusions are as follows:

(1) As the primary raw material of the blast furnace, sintered ore particle has low cost, high-temperature resistance, high strength, and is environmentally friendly and non-toxic. The specific heat of the sinter is 0.86–0.98 J/g/°C in the range of 200–380 °C, which increases with the temperature rising. In addition, due to the unique production process, the sinter has the potential to further improve its thermal properties by optimizing the ratio of raw materials and/or adding other auxiliary materials.

(2) The permeability index JPU in the sintering field can characterize well the airflow resistance characteristics of the sinter bed. A packed bed of small particles has a lower bed permeability and greater air resistance. The permeability first decreases and then gradually stabilizes as air superficial velocity increases.

(3) Due to the smaller voidage and larger specific surface area, the small particle sinter bed has better thermal stratification characteristics and cycle efficiency. Higher charging temperatures lead to sharper thermocline but have no effect on cycle efficiency. The greater air flow speeds up the energy storage cycle, leading to higher cycle efficiency. When the air flow increases from 85 m^3/h to 175 m^3/h, the cycle efficiency increases from 45.90% to 57.60%. When the system gradually enters a stable state, the cycle efficiency can be increased from 57.60% in the first cycle to 66.78%.

(4) The physical properties of solid materials as storage mediums are one of the main factors affecting the storage performances of packed beds. In the next stage, we will compare and analyze the applicability of different materials as sensible heat storage materials. Meanwhile, the effect of different materials on the storage performances of the packed beds will be studied.

Declaration of competing interest

The authors declare that they have no known competing financial interests or personal relationships that could have appeared to influence the work reported in this paper.

Acknowledgements

This work was supported by the National Natural Science Foundation of China (52036008).

References

[1] P. Agrawal, A. Gautam, A. Kunwar, M. Kumar, S. Chamoli, Performance assessment of heat transfer and friction characteristics of a packed bed heat storage system embedded with internal grooved cylinders, Sol. Energy 161 (2018) 148–158.
[2] D. Fernandes, F. Pitié, G. Cáceres, J. Baeyens, Thermal energy storage: "How previous findings determine current research priorities", Energy 39 (2012) 246–257.
[3] S. Kuravi, J. Trahan, D.Y. Goswami, M.M. Rahman, E.K. Stefanakos, Thermal energy storage technologies and systems for concentrating solar power plants, Prog. Energy Combust. Sci. 39 (2013) 285–319.
[4] S.L. Aly, A.I. El-Sharkawy, Effect of storage medium on thermal properties of packed beds, Heat Recovery Syst. CHP 10 (1990) 509–517.
[5] A. Meier, C. Winkler, D. Wuillemin, Experiment for modeling high temperature rock bed storage, Sol. Energy Mater. 24 (1991) 255–264.
[6] D. Okello, O.J. Nydal, E.J.K. Banda, Experimental investigation of thermal destratification in rock bed TES systems for high temperature applications, Energy Convers. Manag. 86 (2014) 125–131.
[7] J. Liu, L. Wang, L. Yang, L. Yue, L. Chai, Y. Sheng, H.S. Chen, C.Q. Tan, Experimental study on heat storage and transfer characteristics of supercritical air in a rock bed, Int. J. Heat Mass Tran. 77 (2014) 883–890.
[8] L. Chai, L. Wang, J. Liu, L. Yang, H.S. Chen, C.Q. Tan, Performance study of a packed bed in a closed loop thermal energy storage system, Energy 77 (2014) 871–879.
[9] G. Zanganeh, A. Pedretti, S. Zavattoni, M. Barbato, A. Steinfeld, Packed-bed thermal storage for concentrated solar power –Pilot-scale demonstration and industrial-scale design, Sol. Energy 86 (2012) 3084–3098.
[10] M. Hänchen, S. Brückner, A. Steinfeld, High-temperature thermal storage using a packed bed of rocks-Heat transfer analysis and experimental validation, Appl. Therm. Eng. 31 (2011) 1798–1806.

[11] A. Mawire, S.H. Taole, A comparison of experimental thermal stratification parameters for an oil/pebble-bed thermal energy storage (TES) system during charging, Appl. Energy 88 (2011) 4766–4778.
[12] D. Schlipf, P. Schicktanz, H. Maier, G. Schneider, Using sand and other small grained materials as heat storage medium in a packed bed HTTESS, International Conference on Concentrating Solar Power and Chemical Energy Systems, Solar PACES 2014, Energy Proc. 69 (2015) 1029–1038.
[13] M. Nems, A. Nems, K. Gebarowska, The influence of the shape of granite on the heat storage process in a rock bed, Energies 13 (2020) 5662–5677.
[14] M. Nems, Experimental determination of the influence of shape on the heat transfer process in a crushed granite storage bed, Energies 13 (2020) 6725–6740.
[15] M. Nems, A. Nems, P. Pacyga, A granite bed storage for a small solar dryer, Materials 11 (2018) 1969–1984.
[16] L.F. Nicolas, Q. Falcoz, D. Pham Minh, J.F. Hoffmann, A. Meffre, A. Nzihou, V. Goetz, Flexibility and robustness of a high-temperature air/ceramic thermocline heat storage pilot, J. Energy Storage 21 (2019) 393–404.
[17] A. Touzo, R. Olives, G. Dejean, D.P. Minh, M.E. Hafi, J.F. Hoffmann, X. Py, Experimental and numerical analysis of a packed-bed thermal energy storage system designed to recover high temperature waste heat: an industrial scale up, J. Energy Storage 32 (2020) 101894.
[18] Mohammad M.S. Al-Azawii, D. Jacobsen, P. Buen, R. Anderson, Experimental study of thermal behavior during charging in a thermal energy storage packed bed using radial pipe injection, Appl. Therm. Eng. 180 (2020) 115804.
[19] R. Daschner, S. Binder, M. Mocker, Pebble bed regenerator and storage system for high temperature use, Appl. Energy 109 (2013) 394–401.
[20] Y. Wang, F.W. Bai, Z.F. Wang, Hiroaki Kiriki, M.X. Han, Shuichi Kubo, Experimental research of the heat transfer characteristics using a packed-bed of honeycomb ceramic for high temperature thermal storage system, International Conference on Concentrating Solar Power and Chemical Energy Systems, Solar PACES 2014, Energy Proc. 69 (2015) 1059–1067.
[21] B. Yang, F.W. Bai, Y. Wang, Z.F. Wang, Study on standby process of an air-based solid packed bed for flexible high-temperature heat storage: experimental results and modelling, Appl. Energy 238 (2019) 135–146.
[22] M. Cascetta, G. Cau, P. Puddu, F. Serra, A study of a packed-bed thermal energy storage device: test rig, experimental and numerical results, 69th Conference of the Italian Thermal Engineering Association, ATI 2014, Energy Procedia 81 (2015) 987–994.
[23] M. Cascetta, F. Serra, G. Cau, P. Puddu, Comparison between experimental and numerical results of a packed-bed thermal energy storage system in continuous operation, Energy Proc. 148 (2018) 234–241.
[24] A. Gautam, R.P. Saini, Experimental investigation of heat transfer and fluid flow behavior of packed bed solar thermal energy storage system having spheres as packing element with pores, Sol. Energy 204 (2020) 530–541.
[25] B. Kocak, A.I. Fernandez, H. Paksoy, Benchmarking study of demolition wastes with different waste materials as sensible thermal energy storage, Sol. Energy Mater. Sol. Cell. 219 (2021) 110777.
[26] B. Kocak, H. Paksoy, Performance of laboratory scale packed-bed thermal energy storage using new demolition waste based sensible heat materials for industrial solar applications, Sol. Energy 211 (2020) 1335–1346.
[27] J.Y. Jang, Y.W. Chiu, 3-D Transient conjugated heat transfer and fluid flow analysis for the cooling process of sintered bed, Appl. Therm. Eng. 29 (2009) 2895–2903.
[28] Y. Liu, J. Yang, J. Wang, Z.L. Cheng, Q.W. Wang, Energy and exergy analysis for waste heat cascade utilization in sinter cooling bed, Energy 67 (2014) 370–380.
[29] F.Y. Tian, L.F. Huang, L.W. Fan, Y.K. Weng, X.Y. Ying, Z.T. Yu, K.F. Cen, A comprehensive characterization on the structural and thermophysical properties of sintered ore particles toward waste heat recovery applications, Appl. Therm. Eng. 90 (2015) 1007–1014.
[30] F.Y. Tian, L.F. Huang, L.W. Fan, H.L. Qian, J.X. Gu, Z.T. Yu, Y.C. Hu, J. Ge, K. F. Cen, Pressure drop in a packed bed with sintered ore particles as applied to sinter coolers with a novel vertically arranged design for waste heat recovery, J. Zhejiang Univ. - Sci. 17 (2016) 89–100.
[31] F.Y. Tian, L.F. Huang, L.W. Fan, H.L. Qian, Z.T. Yu, Wall effects on the pressure drop in packed beds of irregularly shaped sintered ore particles, Powder Technol. 301 (2016) 1284–1293.
[32] E.A. Foumeny, H.A. Moallemi, C. Mcgreavy, J.A.A. Castro, Elucidation of mean voidage in packed beds, Can. J. Chem. Eng. 69 (1991) 1010–1015.
[33] H. Freund, T. Zeiser, F. Huber, E. Klemm, G. Brenner, Fr Durst, G. Emig, Numerical simulations of single phase reacting flows in randomly packed fixed-bed reactors and experimental validation, Chem. Eng. Sci. 58 (2003) 903–910.
[34] H. Zhou, Z.Y. Lai, L.Q. Lv, H. Fang, H.X. Meng, M.X. Zhou, K.F. Cen, Improvement in the permeability of sintering beds by drying treatment after granulating sinter raw materials containing concentrates, Adv. Powder Technol. 31 (2020) 3297–3306.
[35] A.L. Avila-Marin, M. Alvarez-Lara, J. Fernandez-Reche, A regenerative heat storage system for central receiver technology working with atmospheric air, Solar PACES 2013, Energy Procedia 49 (2014) 705–714.
[36] R. Majumdar, S.K. Saha, Computational study of performance of cascaded multi-layered packed-bed thermal energy storage for high temperature applications, J. Energy Storage 32 (2020) 101930.
[37] J. Fernandez-Seara, F.J. Uhıa, J. Sieres, Experimental analysis of a domestic electric hot water storage tank. Part II: dynamic mode of operation, Appl. Therm. Eng. 27 (2007) 137–144.
[38] R.J. Moffat, Describing the uncertainties in experimental results, Exp. Therm. Fluid Sci. 1 (1) (1988) 3–17.
[39] J.S. Feng, H. Dong, H.D. Dong, Modification of Ergun's correlation in vertical tank for sinter waste heat recovery, Powder Technol. 280 (2015) 89–93.
[40] J.S. Feng, H. Dong, J.Y. Liu, K. Liang, J.Y. Gao, Experimental study of gas flow characteristics in vertical tank for sinter waste heat recovery, Appl. Therm. Eng. 91 (2015) 73–79.